REPORT DOCUMENTATION PAGE

Form Approved OMB NO. 0704-0188

1. REPORT DATE (DD-MM-YYYY) 12-12-2016	2. REPORT TYPE Final Report	3. DATES COVERED (From - To) 2-Apr-2015 - 1-Oct-2016

4. TITLE AND SUBTITLE
Final Report: Cross-linked Metal Particles for Low-noise Bolometer Materials

5a. CONTRACT NUMBER
W911NF-15-1-0117

5b. GRANT NUMBER

5c. PROGRAM ELEMENT NUMBER
611102

5d. PROJECT NUMBER

5e. TASK NUMBER

5f. WORK UNIT NUMBER

6. AUTHORS
Zhi-Gang Yu

7. PERFORMING ORGANIZATION NAMES AND ADDRESSES
Washington State University
423 Neill Hall

Pullman, WA 99164 -3140

8. PERFORMING ORGANIZATION REPORT NUMBER

9. SPONSORING/MONITORING AGENCY NAME(S) AND ADDRESS (ES)
U.S. Army Research Office
P.O. Box 12211
Research Triangle Park, NC 27709-2211

10. SPONSOR/MONITOR'S ACRONYM(S)
ARO

11. SPONSOR/MONITOR'S REPORT NUMBER(S)
67021-EL.6

12. DISTRIBUTION AVAILIBILITY STATEMENT
Approved for Public Release; Distribution Unlimited

13. SUPPLEMENTARY NOTES
The views, opinions and/or findings contained in this report are those of the author(s) and should not contrued as an official Department of the Army position, policy or decision, unless so designated by other documentation.

14. ABSTRACT

This final report summarizes WSU's progress from 4/2/2015 to 09/30/2016 on the project, "Cross-linked Metal Particles (CLMPs) for Low-noise Bolometer Materials" funded by the US Army Research Office under Contract # W911NF-15-1-0117. We have successfully carried out the tasks listed in our proposal and gained significant insight into electrical transport in these CLMPs. We have successfully synthesized Au nanoparticles with different capping agents, grown good nanoparticle films, and measured

15. SUBJECT TERMS
infrared detection, bolometers, electrical transport, noise, infrared absorption, nanotechnology

16. SECURITY CLASSIFICATION OF:			17. LIMITATION OF ABSTRACT	15. NUMBER OF PAGES	19a. NAME OF RESPONSIBLE PERSON Zhi-Gang Yu
a. REPORT UU	b. ABSTRACT UU	c. THIS PAGE UU	UU		19b. TELEPHONE NUMBER 509-358-7681

Standard Form 298 (Rev 8/98)
Prescribed by ANSI Std. Z39.18

Report Title

Final Report: Cross-linked Metal Particles for Low-noise Bolometer Materials

ABSTRACT

This final report summarizes WSU's progress from 4/2/2015 to 09/30/2016 on the project, "Cross-linked Metal Particles (CLMPs) for Low-noise Bolometer Materials" funded by the US Army Research Office under Contract # W911NF-15-1-0117. We have successfully carried out the tasks listed in our proposal and gained significant insight into electrical transport in these CLMPs. We have successfully synthesized Au nanoparticles with different capping agents, grown good nanoparticle films, and measured temperature-dependent resistance of the nanoparticle films. In addition, working with Prof. A. J. Syllaios at the University of North Texas, we have started characterizing the noise performance of the nanoparticle films. Our results indicate that the CLMPs can simultaneously have a high temperature coefficient of resistivity and a low noise, and therefore have a great potential in the microbolometer technology.

Enter List of papers submitted or published that acknowledge ARO support from the start of the project to the date of this printing. List the papers, including journal references, in the following categories:

(a) Papers published in peer-reviewed journals (N/A for none)

Received		Paper
08/30/2015	1.00	Zhi-Gang Yu. Spin Hall Effect in Disordered Organic Solids, Physical Review Letters, (07 2015): 0. doi: 10.1103/PhysRevLett.115.026601
TOTAL:		1

Number of Papers published in peer-reviewed journals:

(b) Papers published in non-peer-reviewed journals (N/A for none)

Received	Paper
TOTAL:	

Number of Papers published in non peer-reviewed journals:

(c) Presentations

1. Z. G. Yu, Impurity-band transport in organic spin valves, International Chemical Congress of Pacific Basin Societies (Pacifichem) 2015, Honolulu, Hawaii, December 16, 2015.

2. Z. G. Yu, Magneto-optical properties of hybrid organic-inorganic perovskites. American Physical Society 2016 March Meeting, Baltimore, Maryland, March 18, 2016.

3. Z. G. Yu, Spin Hall Effect and Suppression of the Hanle Effect in Disordered Organics, SPINOS VI, Chicago, Illinois, October 17, 2016

Number of Presentations: 3.00

Non Peer-Reviewed Conference Proceeding publications (other than abstracts):

Received Paper

TOTAL:

Number of Non Peer-Reviewed Conference Proceeding publications (other than abstracts):

Peer-Reviewed Conference Proceeding publications (other than abstracts):

Received Paper

TOTAL:

Number of Peer-Reviewed Conference Proceeding publications (other than abstracts):

(d) Manuscripts

Received Paper

TOTAL:

Number of Manuscripts:

Books

Received Book

TOTAL:

Received	Book Chapter
12/12/2016 5.00	Zhi-Gang Yu. Device physics and spin transport in organic spin valves, Singapore: World Scientific Publishing Company, (2017)
TOTAL:	**1**

Patents Submitted

Patents Awarded

Awards

1. Invited speaker, International Chemical Congress of Pacific Basin Societies (Pacifichem) 2015, Honolulu, Hawaii, December 16, 2015.

Graduate Students

NAME	PERCENT_SUPPORTED
FTE Equivalent:	
Total Number:	

Names of Post Doctorates

NAME	PERCENT_SUPPORTED
Ray Gunawidjaja	0.30
FTE Equivalent:	**0.30**
Total Number:	**1**

Names of Faculty Supported

NAME	PERCENT_SUPPORTED	National Academy Member
Zhi-Gang Yu	0.20	
FTE Equivalent:	**0.20**	
Total Number:	**1**	

Names of Under Graduate students supported

NAME	PERCENT_SUPPORTED
FTE Equivalent:	
Total Number:	

Student Metrics

This section only applies to graduating undergraduates supported by this agreement in this reporting period

The number of undergraduates funded by this agreement who graduated during this period: 0.00

The number of undergraduates funded by this agreement who graduated during this period with a degree in science, mathematics, engineering, or technology fields:...... 0.00

The number of undergraduates funded by your agreement who graduated during this period and will continue to pursue a graduate or Ph.D. degree in science, mathematics, engineering, or technology fields:...... 0.00

Number of graduating undergraduates who achieved a 3.5 GPA to 4.0 (4.0 max scale):...... 0.00

Number of graduating undergraduates funded by a DoD funded Center of Excellence grant for Education, Research and Engineering:...... 0.00

The number of undergraduates funded by your agreement who graduated during this period and intend to work for the Department of Defense 0.00

The number of undergraduates funded by your agreement who graduated during this period and will receive scholarships or fellowships for further studies in science, mathematics, engineering or technology fields:...... 0.00

Names of Personnel receiving masters degrees

NAME

Total Number:

Names of personnel receiving PHDs

NAME

Total Number:

Names of other research staff

NAME	PERCENT_SUPPORTED
FTE Equivalent:	
Total Number:	

Sub Contractors (DD882)

Inventions (DD882)

Scientific Progress

See Attachment

Technology Transfer

Final Report

Cross-linked Metal Particles for Low-noise Bolometer Materials

ARO Contract W911NF-15-1-0117

Prepared by:

Zhi-Gang Yu, Senior Scientist
ISP/Applied Sciences Laboratory
Washington State University

Prepared for:

U.S. Army Research Office
P.O. Box 12211
Research Triangle Park, NC 27709-2211

Attention: Dr. William Clark

Abstract

This final report summarizes WSU's progress from 4/2/2015 to 09/30/2016 on the project, "Cross-linked Metal Particles (CLMPs) for Low-noise Bolometer Materials" funded by the US Army Research Office under Contract # W911NF-15-1-0117. We have successfully carried out the tasks listed in our proposal and gained significant insight into electrical transport in these CLMPs. We have successfully synthesized Au nanoparticles with different capping agents, grown good nanoparticle films, and measured temperature-dependent resistance of the nanoparticle films. In addition, working with Prof. A. J. Syllaios at the University of North Texas, we have started characterizing the noise performance of the nanoparticle films. Our results indicate that the CLMPs can simultaneously have a high temperature coefficient of resistivity and a low noise, and therefore have a great potential in the microbolometer technology.

1 Introduction

The objective of this project is to design, fabricate, and characterize a novel bolometer material: cross-linked metal particles (CLMPs). In the CLMPs, the inter-particle distance is regulated by organic ligands that are chemically bonded to adjacent metal particles. According to our modeling results, the temperature coefficient of resistance (TCR) and noise in a CLMP film are determined by the particle size and inter-particle distance, respectively. Hence CLMPs enable independent tuning of the TCR and $1/f$ noise and may revolutionize the search for appropriate microbolometer materials.

This project started from the results of an ARO-funded project when the PI was employed at SRI International. Those previous results indicate that while CLMP films are very promising for low-noise microbolometers, growing thick CLMP films cross-linked with short ligands appears very challenging. To overcome this technical challenge, at the beginning of the project, we designed several strategies and different approaches to ensure a successful growth of high-quality CLMP films. Using these strategies and approaches, we have succeeded in synthesizing Au NPs with several capping agents and growing high-quality CLMP films cross-linked with short ligands, as required from modeling results. We have also characterized the TCR of the CLMP films and, in collaboration with Prof. Syllaios at the University of North Texas, started measuring the noise performance. On the modeling aspect, we have developed a comprehensive modeling tool to calculate electrical transport and infrared absorption properties in CLMP films and to design CLMP films for optimized performance.

2 Comprehensive model of electrical transport and infrared absorption of CLMPs

The most important material properties relevant to microbolometer applications are temperature-dependent electrical conductivity, $1/f$ noise, and infrared absorption. In this project we have developed a comprehensive code that can model these properties effectively. The code includes the following key ingredients.

2.1 Coulomb-energy barrier

When the CLMP film is under bias, electrical transport occurs via electron tunneling between adjacent metal nanoparticles (NPs). In this tunneling process, the two originally neutral metal particles become charged: one with a negative charge and the other with a positive charge. Thus the electron tunneling must overcome the Coulomb-energy barrier between the charged NPs, the Coulomb energy of charging the two particles can be expressed as e^2/C, where C is capacitance between two adjacent particles and is evaluated by considering an infinite series of image charges.

First we examine the energy required to oppositely charge two metal NPs with an infinite inter-particle distance. Since an isolated metal sphere can be considered as a capacitor with a capacitance of $4\pi\epsilon_0\epsilon_b a_i$, where a_i is the radius of the ith sphere and ϵ_b the effective dielectric constant obtained above, the Coulomb energy of charging the two separated NPs is

$$\begin{aligned} E_c^0 &= \frac{e^2}{2C_1} + \frac{e^2}{2C_2} \\ &= \frac{e^2}{8\pi\epsilon_0\epsilon_b}\Big(\frac{1}{a_1} + \frac{1}{a_2}\Big). \end{aligned} \tag{2.1}$$

The Coulomb energy needed to oppositely charge adjacent NPs would be smaller than E_c^0 calculated above because of the interaction between the NPs. Using the image-charge method, we found that the Coulomb energy of charging the two separated NPs can be expressed as

$$E_c = \frac{e^2}{2C} = \frac{e^2(k_{11} + k_{22} + 2k_{12})}{2\epsilon_b(k_{11}k_{22} - k_{12}^2)}. \tag{2.2}$$

where

$$k_{11} = a_1 a_2 \sinh\theta \sum_{n=1}^{\infty} |a_2 \sinh n\theta + a_1 \sinh(n-1)\theta|^{-1}, \tag{2.3}$$

$$k_{12} = -\frac{a_1 a_2}{c} \sinh\theta \sum_{n=1}^{\infty} |\sinh n\theta|^{-1}, \tag{2.4}$$

$$k_{22} = a_1 a_2 \sinh\theta \sum_{n=1}^{\infty} |a_1 \sinh n\theta + a_2 \sinh(n-1)\theta|^{-1}. \tag{2.5}$$

Here $\cosh\theta = (c^2 - a_1^2 - a_2^2)/(2a_1a_2)$with a_1 and a_2 being the radii of the two spheres, c the center-to-center distance between the two spheres, $c = a_1 + a_2 + t$ with t being the edge-to-edge distance (the ligand length), and ϵ_b is the dielectric constant of the organic ligand.

The corresponding capacitance between the two adjacent particles is

$$C = \frac{\epsilon_b(k_{11}k_{22} - k_{12}^2)}{k_{11} + k_{22} + 2k_{12}}. \tag{2.6}$$

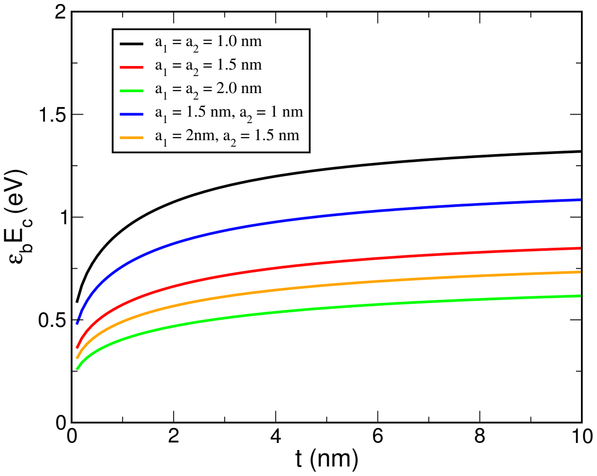

Figure 1: Coulomb energy of oppositely charged NPs as a function of edge-to-edge distance between the particles for different particle sizes.

E^c and C, which depend on the radii of and the distance between the two adjacent particles, are important properties that will affect electrical transport in CLMPs. Figure 1 plots the Coulomb energy between two particles as a function of their edge-to-edge distance.

2.2 Microscopic polarizability of organic ligands

The Coulomb-energy barrier calculated above depends on the dielectric constant of the host material — in this case, the organic ligands connecting the NPs. However, these ligands are molecular monolayers, which renders the usual macroscopic dielectric constant of these organic materials, an ensemble averaged property, inapplicable to the current situation. Instead, one must use microscopic polarizability of individual organic ligands to calculate the Coulomb energy between the charged NPs.

We have employed the Gaussian09 program suite to carry out the polarizability calculations for representative organic ligands that have been used in literature as cross-link agents between metal NPs. Table I lists the obtained polarizability p of these organic molecules and their molecular volume v.

For molecules with a negligible permanent dipole moment, the effective dielectric constant can be calculated from the Clausius-Mossotti equation,

$$\frac{\epsilon_b - 1}{\epsilon_b + 2} = \frac{4\pi}{3v} p. \tag{2.7}$$

Table 1: Volume (v), polarizability (p), and effective dielectric constant (ϵ_b) of cross-link organic molecules. r_0 is the Bohr radius.

Molecule	v (r_0^3)	α (r_0^3)	ϵ_b
$C_{10}N_8H_6S_4O_2$	2760.955	4.846e+02	9.34
$C_{12}H_{10}S_3$	1942.358	3.057e+02	6.08
$C_{24}H_{18}S_6$	4285.346	6.925e+02	7.29
$C_{28}N_2H_2O$	3459.573	8.448e+02	4.53
$C_6H_6S_2$	1280.082	1.678e+02	4.65
$C_8H_{10}S_2$	1499.479	1.922e+02	4.48
PPh_3	2433.059	2.544e+02	3.34

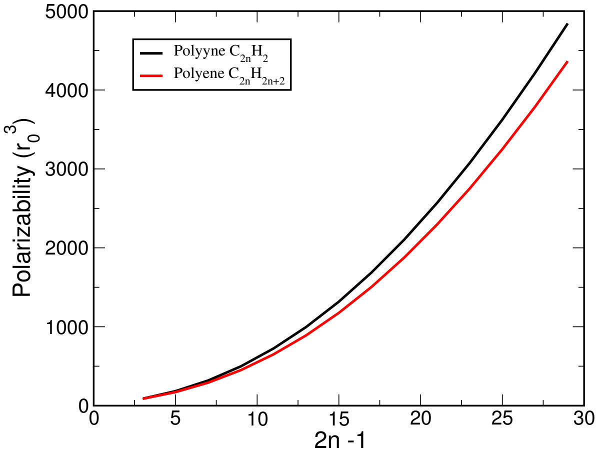

Figure 2: Polarization as a function of length of molecules.

For molecules with a sizable permanent dipole moment μ, the Lorentz-Debye equation should be used,

$$\frac{\epsilon_b - 1}{\epsilon_b + 2} = \frac{4\pi}{3v}\Big(p + \frac{\mu^2}{3k_B T}\Big), \tag{2.8}$$

where T is the temperature and k_B the Boltzmann constant. Using these equations, we calculate the effective dielectric constant ϵ_b for the organic molecules and list them in Table I. The obtained ϵ_b will be used to evaluate the Coulomb-energy barrier of electron tunneling between adjacent NPs.

We emphasize that the obtained ϵ_b would in general be different from the dielectric constant of a thick film of these molecules. In fact, the polarizability is not proportional to the system size, as shown in Figure 2, which plots the polarizabilities of polyyne and polyene molecules, both chain-like, versus the molecular length. It is clear that the polarizability depends on the molecular length nonlinearly.

2.3 Electron tunneling between two adjacent particles

To study electrical transport, we consider the basic continuity equation (charge conservation) at a given metal particle,

$$q\frac{dn_i}{dt} = -\sum_j (I_{ij} - I_{ji}), \tag{2.9}$$

where n_i is the electron density in the ith particle, and I_{ij} is the electrical current flowing from particle i to particle j.

When a CLMP film is under a bias, individual particles have a different potential, V_i for particle i. Then the electron tunneling current from occupied states in particle i to unoccupied states in particle j is

$$I_{ij} = \int dEpe^{-2\chi t_{ij}} f(E)[1 - f(E + q(V_j - V_i) - E^c_{ij})], \tag{2.10}$$

where $f(E) = [1 + e^{E/k_BT}]^{-1}$ is the Fermi-Dirac distribution, p is normalization constant, t_{ij} is the edge-to-edge separation between particles i and j, E^c_{ij} is the Coulomb energy of charging particles i and j obtained earlier, and $\chi = [2m(\phi - E)]^{1/2}/\hbar$ is the tunneling factor obtained from the WKB approximation with ϕ and m being the metal work function and the electron mass. Here we set the electrochemical potential (Fermi energy) of the particle i to be zero. This expression describes two competing factors that influence the electron tunneling: One is the potential difference between the two particles in the presence a bias, which facilitates electron tunneling; the other is the Coulomb energy of charging the two particles (because after the tunneling, particle j becomes negatively charged and particle i becomes positively charged), which hinders electron tunneling.

Conversely, the electron tunneling current from particle j to particle i is

$$I_{ji} = \int dEpe^{-2\chi t_{ij}} f(E + q(V_j - V_i))[1 - f(E - E^c_{ij})]. \tag{2.11}$$

The basic tunneling probability is evaluated at finite temperature and at arbitrary voltage difference.

2.4 Electrical transport in a network of particles

To calculate the I-V characteristics of the CLMP film, we need to consider a 3d network of metal particles and solve the steady-state equations,

$$0 = \sum_j (I_{ij} - I_{ji}), \tag{2.12}$$

where

$$I_{ij} = pe^{-2\chi t_{ij}} \frac{q(V_j - V_i) - E_{ij}^c}{1 - e^{\beta[q(V_j - V_i) - E_{ij}^c]}}, \tag{2.13}$$

$$I_{ji} = pe^{-2\chi t_{ij}} \frac{q(V_j - V_i) + E_{ij}^c}{e^{\beta[q(V_j - V_i) + E_{ij}^c]} - 1}. \tag{2.14}$$

These equations are highly nonlinear and the number of equations is enormous (we are currently doing 32×32×32).

Under a low bias, the expressions of I_{ij} and I_{ji} can be linearized. The obtained linear equations can be efficiently solved by using the sparse-matrix technique.

Obtaining a stable solutions for these nonlinear equations is very challenging. We have developed a numerical algorithm, in which we gradually increase the applied voltage

$$V_i = V_i^0 + \delta V_i, \tag{2.15}$$

where V_i^0 is the solution to the equations for an applied bias of V^0, and V_i is the solution to be found when the bias increases by δV, $V = V^0 + \delta V$. We make $q\delta V \ll k_B T$, and thus δV_i is small as compared with V_i^0. We linearize the equations around V_i^0, and the above nonlinear equations become linear equations of δV_i

$$\begin{aligned}
& \sum_j pe^{-2\chi t_{ij}} (\delta V_j - \delta V_i) \Big[\frac{q}{1 - e^{-\beta[q(V_j^0 - V_i^0) - E_{ij}^c]}} - \frac{q}{e^{\beta[q(V_j^0 - V_i^0) + E_{ij}^c]} - 1} \\
- & \quad \frac{q^2 \beta [q(V_j^0 - V_i^0) - E_{ij}^c] e^{-\beta[q(V_j^0 - V_i^0) - E_{ij}^c]}}{[1 - e^{-\beta[q(V_j^0 - V_i^0) - E_{ij}^c]}]^2} + \frac{q^2 \beta [q(V_j^0 - V_i^0) + E_{ij}^c] e^{\beta[q(V_j^0 - V_i^0) + E_{ij}^c]}}{[e^{\beta[q(V_j^0 - V_i^0) + E_{ij}^c]} - 1]^2} \Big] \\
= & \quad - \sum_j pe^{-2\chi t_{ij}} \Big[\frac{q(V_j^0 - V_i^0) - E_{ij}^c}{1 - e^{-\beta[q(V_j^0 - V_i^0) - E_{ij}^c]}} + pe^{-\chi t_{ij}} \frac{q(V_j^0 - V_i^0) + E_{ij}^c}{e^{\beta[q(V_j^0 - V_i^0) + E_{ij}^c]} - 1} \Big],
\end{aligned} \tag{2.16}$$

which can be solved by using the sparse matrix techniques and the conjugated gradient method.

Figures 3 and 4 plot current as a function of the inverse of applied bias for CLMP films at different temperatures. It is seen that the I-V curves are highly nonlinear as

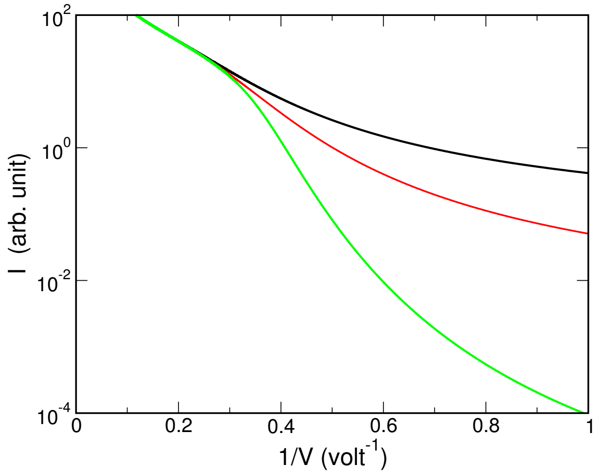

Figure 3: Current vs inverse of bias in CLMPs for $\epsilon_b = 2$. Black, red, and green curves correspond to $T = 300$, 200, and 100 K, respectively. The parameters are $a = 2$ nm and $t = 0.5$ nm.

the applied bias increases. There is a clear crossover, above which the I-V characteristics become independent of temperature. This crossover occurs when the electron energy gain due to the voltage drop overcomes the Coulomb energy of charging two adjacent particles. Thus the Coulomb energy can be obtained from the voltage dependence at a fixed temperature and from the temperature dependence under a small voltage. In the high-bias regime, the logarithm of current depends linearly on $1/V$, suggesting that

$$I \sim \exp(-V_c/V), \tag{2.17}$$

where the characteristic bias V_c is the bias at which the Coulomb energy $\langle E^c_{ij} \rangle$ is the same as energy gain due to the potential difference, $\langle q\frac{V_c}{L}(a_i + a_j + t) \rangle$, with L being the length between the two electrodes.

Figures 3 and 4 also show that strong temperature dependence of electrical transport is at low bias, and that to achieve high temperature sensitivity, a large $\langle E^c_{ij} \rangle$ is needed. Thus the Coulomb energy can be obtained from the voltage dependence at a fixed temperature and from the temperature dependence under a small voltage.

2.5 AC transport

The AC transport introduces another time scale, i.e., the time period the AC voltage. In addition, at a finite frequency, both electrical tunneling and displacement current in a

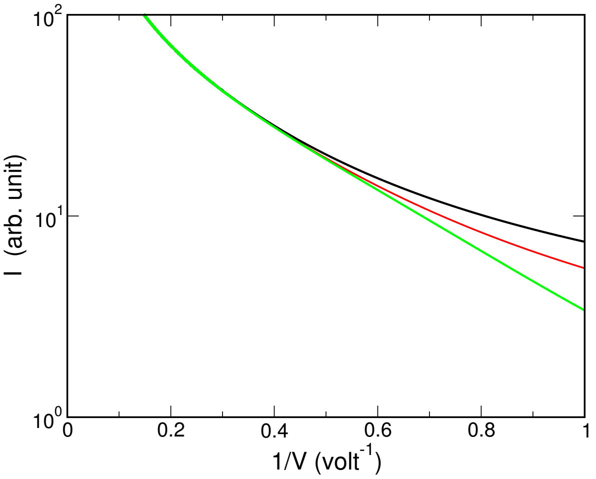

Figure 4: Current vs inverse of bias in CLMPs for $\epsilon_b = 6$. Black, red, and green curves correspond to $T = 300$, 200, and 100 K, respectively. The parameters are $a = 2$ nm and $t = 0.5$ nm.

capacitor between any two adjacent particles contribute to electrical transport. Thus the AC transport would also reveal information on the capacitance between adjacent particles, which depends on the particle size and the inter-particle distance.

To study the AC transport, one need to solve time-dependent equations.

$$q\frac{dn_i}{dt} = \sum_j (I_{ji} - I_{ij}). \tag{2.18}$$

At low bias, $|q(V_j - V_i)| \ll k_B T$, the AC transport problem is reduced to an impedance network problem. For an AC bias with frequency of ω, $V(t) = Ve^{-i\omega t}$, the above equations reduce to

$$0 = \sum_j (V_j - V_i) Z_{ij}^{-1}, \tag{2.19}$$

with an impedance between each pair of adjacent particles,

$$Z_{ij}^{-1}(\omega) = R_{ij}^{-1} + i\omega C_{ij}, \tag{2.20}$$

$$C_{ij} = \frac{\epsilon_b k_{11} k_{22} - k_{12}^2}{k_{11} + k_{22} + 2k_{12}}, \tag{2.21}$$

$$R_{ij}^{-1} = pe^{-2\chi t_{ij}} e^{-\chi t_{ij}} \frac{2}{1 - e^{\beta E_{ij}^c}}. \tag{2.22}$$

In deriving Eq. (2.20), we have neglected the Fermi energy change in each metal particle of the CLMP film under a small AC voltage.

To solve these complex-coefficient linear equations, we first treat the real and imaginary parts of complex V_i as two independent real variables and rewrite these equations as real-coefficient linear equations. The matrix size changes from $N \times N$ to $2N \times 2N$. We find that the conjugated gradient approach is not numerically reliable. So we have employed the generalized minimal residual algorithm, together with sparse-matrix technique to solve these equations and find complex V_i. Then we compute the total current I and obtain the AC conductance $\sigma(\omega)$ via $\sigma(\omega) = I(\omega)/V(\omega)$.

Figure 5 plots both the real part and the modulus of σ as a function of frequency ω. We see that $|\sigma(\omega)|$ depends only weakly on the frequency at low frequencies, then takes off at a critical frequency, increasing linearly with the frequency. The underlying physics is that at low frequencies, the displacement current through the capacitance is negligible as compared to the tunneling current, electrical transport is due mainly to tunneling, which is independent of frequency. As the frequency increases, the displacement current becomes more important, and at the critical point, is comparable to the tunneling current. After that, the displacement current is dominant. In the figure, the slope of $|\sigma(\omega)|$ at large ω is determined by the effective capacitance of the system. Thus from impedance measurement of an CLMP film, we should be able to extract the information of the average capacitance and tunneling current between adjacent particles. Since they both depend on the particle size and the inter-particle distance, the AC transport measurement could serve as a diagnostic tool to independently determine the particle size and volume loading density in a CLMP film.

2.6 Noise

Noise is critical to the performance of a microbolometer. In fact, the sensitivity of existing microbolometers based on VO$_x$ and α-Si is limited by the $1/f$ noise in these systems. In general, the noise originates from the diverse timescales associated with the electron tunneling between adjacent NPs.

The model also systematically calculates the noise level by solving the time-dependent master equation, in the present of a temporal fluctuation, $\eta_i(t)$,

$$\frac{d\delta\mu_i}{dt} = -\sum_j [w_{ij}(\delta\mu_i - \delta\mu_j)] - \eta_i(t), \tag{2.23}$$

where

$$w_{ij} = \gamma \frac{e^2 \Gamma \bar{a}^2}{4\pi t} e^{-2\Gamma t} e^{-E_c^{ij}/k_B T}. \tag{2.24}$$

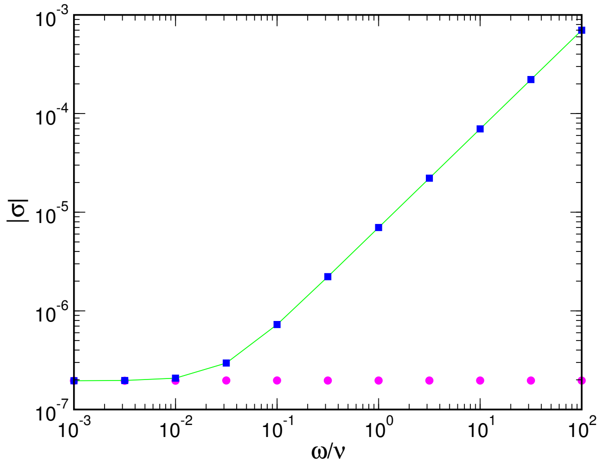

Figure 5: AC conductance of CLMP film as a function of frequency. Circles and squares correspond to $\mathrm{Re}\sigma(\omega)$ and $|\sigma(\omega)|$, respectively.

The master equation can be written as a matrix form,

$$\frac{d\delta\mu_i}{dt} = \sum_j A_{ij}\delta\mu_j - \eta_i, \tag{2.25}$$

where the matrix $\boldsymbol{A}$ is

$$A_{ij} = -\sum_k w_{ik}\delta_{ij} + w_{ij}. \tag{2.26}$$

Denoting the kth eigenvalue of $\boldsymbol{A}$ as λ_k and its associated eigenvector as $\boldsymbol{\xi}_k$, the spectral density of fluctuations, according to the Wiener-Khintchine theorem, is

$$P_k(\omega) = 2\overline{\tilde{\xi}_k(\omega)\tilde{\xi}_k(-\omega)} = \frac{2D_k}{\omega^2 + \lambda_k^2} \tag{2.27}$$

where D_k is the averaged intensity of the random pulses, and can be determined by the equipartition law, that the chemical-potential (voltage) fluctuation in a circuit is

$$\frac{1}{2}C\overline{\xi_k^2} = \frac{1}{2}k_BT = \int_0 P_k(\omega)d\omega = \frac{D_k}{2\lambda_k}, \tag{2.28}$$

where C is the average capacity of the circuit. The total spectral density, including all the modes, is then

$$P(\omega) = \sum_k P_k(\omega) = \sum_k \frac{4k_BT}{C}\frac{\lambda_k}{\omega^2 + \lambda_k^2}. \tag{2.29}$$

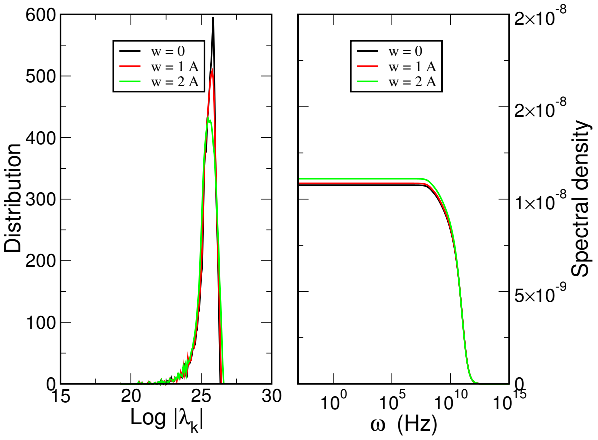

Figure 6: Distribution of logarithm of eigenvalue (left panel) and noise spectral density for CLMPs with different size fluctuation density.

Thus to calculate the noise spectrum, we need to find all the eigenvalues of the matrix $\boldsymbol{A}$. It is easy to see that one eigenvalue is $\lambda_0 = 0$, which corresponds to the equilibrium situation. All other eigenvalues must be negative, $\lambda_k < 0$, because any fluctuation will decay over time. We have considered a large CLMP system consisting of $32 \times 16 \times 16$ metal NPs, and computed all eigenvalues λ_k as well the noise spectral density for different particle size fluctuations, as shown in Figure 6. We see that $1/\lambda_k$, which describes microscopic time scales, has a very narrow distribution as compared to disordered VO$_x$. Hence the noise level in CLMPs is much lower than that in disordered materials like VO$_x$. More important, the noise level becomes saturated at low frequencies and does not increase indefinitely as the frequency is lowered. Thus the CLMPs would have a very low noise level.

2.7 Infrared absorption

Since a microbolometer is used to detect infrared radiation, it is important to understand the IR response of the CLMP films between 8 to 14 microns. When the active bolometer material is a good IR absorber, the microbolometer architecture can be greatly simplified. Our model also computes the IR response of CLMP films, which can be considered as metal NPs embedded in an organic host. The effective dielectric response of this composite system usually can be computed from the well-known Maxwell-Garnett theory and the Mie solution.

Table 2: n and k in the infrared region of Au bulk

wavelength (μm)	n	k
7.999	8.5	46.4
8.266	9.016	47.6
8.551	9.582	48.8
8.856	10.21	50.2
9.184	10.84	51.6
9.537	11.51	53.1
9.919	12.24	54.7

$$\epsilon_{\text{eff}}(\omega) = \epsilon_1(\omega)\Big(1 + \frac{3f}{\frac{\epsilon_p(\omega)+2\epsilon_1(\omega)}{\epsilon_p(\omega)-\epsilon_1(\omega)} - f}\Big), \tag{2.30}$$

where ϵ_1 is the dielectric response of the host (organic) material, f is the volume fraction of NPs in the composite,

$$f = \frac{4\pi}{3}\frac{\bar{a}^3}{(2\bar{a}+t)^3}, \tag{2.31}$$

and ϵ_p is related to the dielectric function of metal ϵ_2 via

$$\frac{\epsilon_p}{\epsilon_2} = F(x) \equiv \frac{2(\sin x - x\cos x)}{x^2-1)\sin x + x\cos x}, \tag{2.32}$$

with $x = ka\sqrt{\epsilon_2\mu_2}$ and k being the wave vector.

We use the measured dielectric function of bulk Au to describe ϵ_2. In literature, the available n and k in the infrared region for Au are listed in Table 2. We interpolate these measured values to obtain n and k for other wavelengths.

Special caution must be taken when describing the dielectric function of the host (organic) material. Usually, an insulating bulk organic material does not strongly absorb the IR radiation. In CLMPs, however, the organic ligand is not an electric insulator, for electrons can tunnel between adjacent metal NPs. Thus the organic material in CLMPs do have an effective conductivity. In addition, as discussed earlier, there is a capacitance C between each pair of adjacent NPs, which also facilitates electrical conduction at finite frequencies. Hence the effective resistivity of the organic ligand between the two adjacent NPs at frequency ω is

$$\rho_e = \rho_t\frac{2at}{A}\Big(1 + i\omega C\rho_t\frac{t}{A}\Big)^{-1}, \tag{2.33}$$

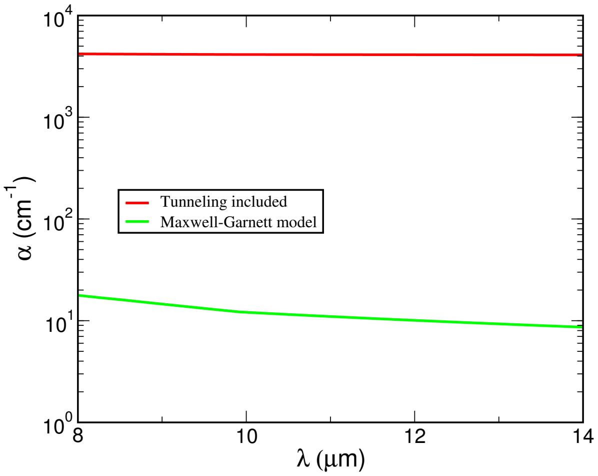

Figure 7: IR absorption spectrum of CLMPs. The parameters are $a = 2$ nm and $t = 0.5$ nm.

where A is the effective tunneling area with the non-planar nature of spheres included, $A = \pi a/\Gamma$, and $\rho_t = 1/\sigma$ with σ from Eq. (2.22).

The equivalent dielectric function of the organic ligands in CLMP films is then

$$\epsilon_1(\omega) = \epsilon_b + \frac{4\pi i}{\omega\rho_e} = \epsilon_b + \frac{2\pi}{a}\Big(C + i\frac{A}{\omega\rho_t t}\Big). \tag{2.34}$$

Substituting Eq. (2.34) into Eq. (2.30), we obtain the effective dielectric function for the composite, the CLMP films. The absorption spectrum can be computed from

$$\alpha(\omega) = \frac{4\pi}{\lambda}k = \frac{4\pi}{\lambda}\sqrt{\frac{1}{2}\Big[|\epsilon_{\text{eff}}(\omega)| - \text{Re}\epsilon_{\text{eff}}(\omega)\Big]} \tag{2.35}$$

The calculated IR absorption spectrum is illustrated in Figure 7. We see that the IR absorption is greatly enhanced when the tunneling conduction is included. Without the tunneling contribution, as illustrated by the green line, the IR absorption would be very weak. Our results suggest a strong IR absorption in CLMP films where electron tunneling between adjacent NPs is significant.

3 Synthesis of NPs and growth of NP films

In the proposed CLMP structure, metal particles are separated by organic ligands that form chemical bonds to the metal particles at the both ends (cross-linking). We have tried

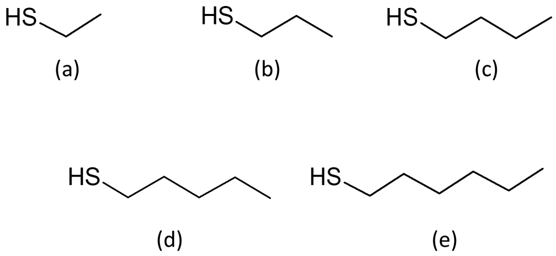

Figure 8: Chemical structures of: (a) ethanethiol, (b) propanethiol, (c) butanethiol, (d) pentanethiol, and (e) hexanethiol.

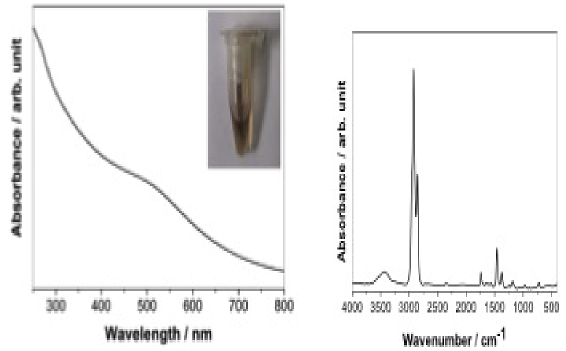

Figure 9: UV/Vis absorption spectrum of Au-C_6 nanoparticles in hexanes. Inset shows the Au NP dispersion. (b) The corresponding FTIR spectrum in a KBr pellet.

many different synthesis and film-growth routes. Here we summarize the approaches that worked. For an easy reference, we display in Figure 8 the molecular structures of the capping agents used in this report.

3.1 Synthesis of Au NPs capped with 1-hexanethiol

We synthesized Au NPs from $HAuCl_{4.3}H_2O$ and capped these NPs with 1-hexanethiol. The obtained capped NPs, named as Au-C_6, are purified by multiple precipitation/re-dispersion cycles with toluene as the solvent and ethanol as the precipitating medium.

Figure 9a shows the UV/Vis spectrum of the 1-hexanethiol capped Au NPs in hexanes. A weak hump, caused by the plasmon resonance of the Au NPs, is seen between 400 and 600 nm. The weak plasmon resonance is consistent with the small diameter of NPs. Figure

9b shows the corresponding FTIR spectrum. The observation of the prominent peak at 1462 cm^{-1} confirms the presence of 1-hexanethiol. The absence of the S-H vibrational peak between 2600 and 2550 cm^{-1} indicates that 1-hexanethiols are adsorbed onto the Au NPs surface.

3.2 Synthesis of Au NPs capped with ethanethiol

From our modeling results, in the Au NP film cross-linked with 1,9-nonanedithiol, the distance between Au particles, which is the molecular length of 1,9-nonanedithiol, is too long for the film to be a semiconductor. For the bolometer applications, we need to cross link the NPs with much shorter ligands, like benzene-1,4-dithiol, which requires Au NPs capped with a short agent, such as ethanethiol, be synthesized.

We tried to synthesize the ethanethiol functionalized Au NPs, named as Au-C_2, in the same way as Au-C_6 described above, except that chloroform is used as the solvent. The use of a shorter ligand, ethanethiol in place of 1-hexanethiol in Au-C_6, however, yielded much larger sized NPs, as indicated by the more pronounced plasmon absorption between 400 and 600 nm.

Facing the upset, we tried another approach among our developed strategies and approaches. That is to first synthesize triphenyl phosphine (TPP) capped NPs, named as Au-TPP. The Au-TPP then could undergo a ligand exchange with ethanethiol, giving rise to Au-C_2.

The protocol for preparing Au-TPP is done according to the procedure reported by Woehrle [2]. Au-TPP is formed by addition of $NaBH_4$ to a solution of AuCl(TPP) in ethanol. The product is isolated by precipitation in hexanes, followed by filtration. It is then rinsed with hexanes, CH_2Cl_2/hexanes (1:1), and CH_2Cl_2/hexanes (3:1).

Figure 10 shows UV/Vis spectrum of the obtained Au-TPP in a dilute $CHCl_3$ solution. The weak hump between 500 and 550 nm suggests a small diameter of the Au NPs. The overall appearance of the spectrum is in agreement with that reported in the literature [2].

To make Au-C_2, the obtained Au-TPP NPs are dissolved in chloroform and then ethanethiol is added into the solution at equal mass with Au-TPP. The product is isolated via precipitation in hexanes. Figure 10b compares the UV/Vis spectrum of Au-TPP with Au-C_2. The weakening of the peak at 308 nm indicates the removal of the TPP group in Au-C_2.

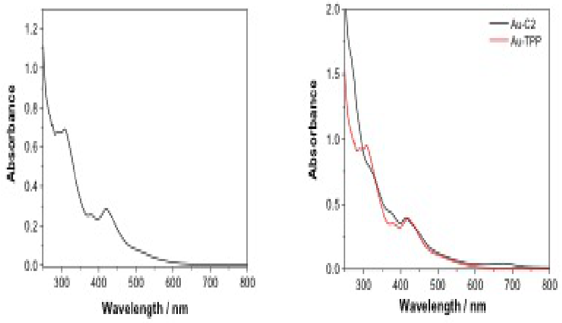

Figure 10: (a) UV/Vis absorption spectrum of Au-TPP in a dilute $CHCl_3$ solution. (b) Comparison of UV/Vis spectra of Au-TPP and Au-C_2.

3.3 Growth of CLMP films

To ensure good film formation, the glass substrate was treated with piranha solution (1/3 sulfuric acid/hydrogen peroxide mixture) to enrich the surface with hydroxyl groups. It is then rinsed with abundant deionized water and acetone. Next, the glass substrate was functionalized with n-octyltriethoxysilane.

Following the protocol described in [1], 25 μL of Au-C_6 solution in heptane is drop casted onto the n-octyltriethoxysilane functionalized glass substrate. The spin-coated film is then cross-linked by soaking in a solution of 1,9-nonanedithiol. Figure 11 shows the obtained Au-C_6 films and the small particle size is corroborated by the UV/Vis absorption spectra.

To grow good Au-C_2 films, again, the treatment to the glass substrate is essential. We then spin-coated the precipitated Au-TPP on the n-octanetriethoxysilane functionalized glass substrate. The film was subsequently treated with benzene 1,4-dithiol, the desired short ligand, for cross-linking.

Figure 12 shows the UV/Vis absorption of the cross-linked film. The absorption peak within 500 and 550 nm is not seen, suggesting that the Au NPs diameter is small. The film image, displayed in the inset, demonstrates the quality and uniformity of the film. Figure 12b is the corresponding reflectance spectrum, which can be fitted to allow film thickness estimation. The estimated film thickness is around several hundred nanometers.

To estimate the thickness of the films, we used the Atomic Force Microscopy (AFM) and measured the film thickness. The thickness range is between 100-500 nm.

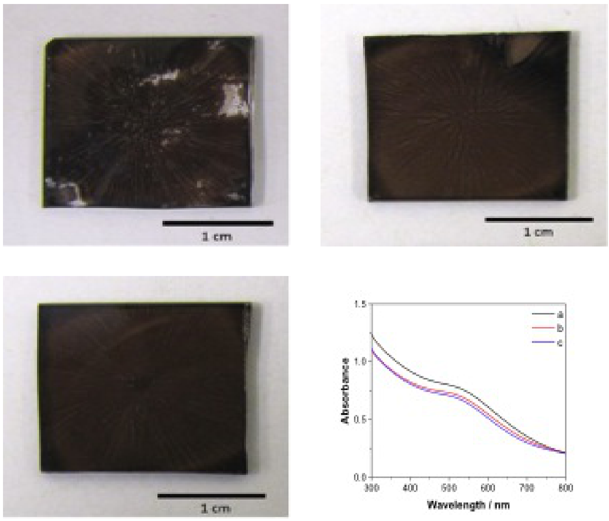

Figure 11: Pictures of Au-C_6 film spin-coated on an n-octyltriethoxysilane functionalized glass substrate, subsequently cross-linked with 1, 9-nonanedithiol in (a) 1-butanol and (b,c) isopropanol. (d) The corresponding UV/Vis absorbance spectra.

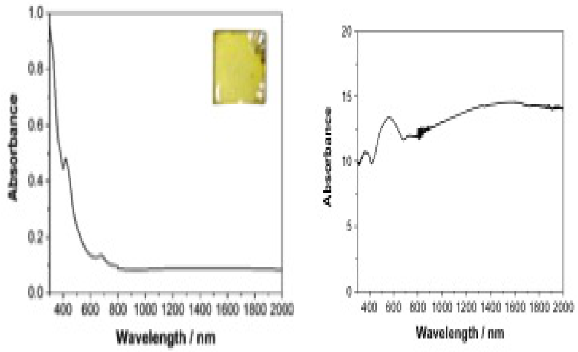

Figure 12: (a) UV/Vis spectrum of Au-C_2 spin coated from a 50mg/mL solution in CHCl3, subsequently treated with benzene 1,4-dithiol in hexane. (b) The corresponding reflectance spectrum.

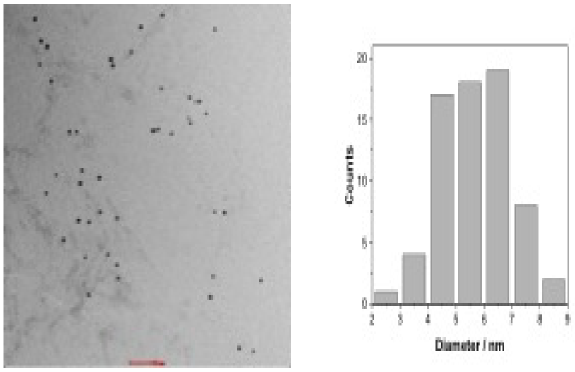

Figure 13: TEM images of Au-C_2 taken at (a) 80K magnification and (b) size distribution.

3.4 TEM Images and size of Au NPs

Having made the films of Au-C_6 and Au-C_2, it is critical to check on the NPs size. The three types of Au-NPs that had been prepared i.e., (1) Au-C_2, (2) Au-C_6, and (3) Au-TPP were sent out for TEM imaging at Franceschi Microscopy & Imaging Center (WSU-Pullman).

3.4.1 Au-C_2

Direct particle size measurements from its TEM images shows that the diameter of Au-C_2 is about 5.7 ± 1.2 nm (Figure 13). The Au-C_2 NPs are obtained by performing ligand exchange of Au-TPP with ethanethiol. Au-TPP is known to be unstable due to the weak interaction with the capping agent TPP. It is possible that the NP size grows from the initial < 5 nm size to about 5.7 ± 1.2 nm either during storage or during the ligand exchange reaction.

3.4.2 Au-C_6

Due to the poor contrast, the particle-size measurement is less straightforward for Au-C_6, but from Figure 14 below it is seen that the diameters are less than 5 nm.

3.4.3 Au-TPP

Based on limited number of particles, the average particle size derived from Figure 15 below is for Au-TPP is about 2.4 ± 1.0 nm. This size is ideal for bolometer applications from our modeling results. The increase in Au NP size from Au-TPP to Au-C_2 may

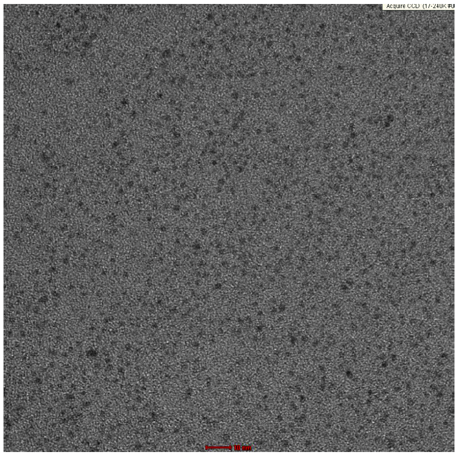

Figure 14: TEM images of Au-C6 obtained at 240K magnification.

take place during either the storage or the ligand exchange process, as mentioned above. Currently we are working on the conditions that prevent such size change from happening.

4 Electrical-transport measurements

We have put together a PID (Proportional, Integral, Derivative) controlled heater strip to enable temperature controlled experiments between ambient temperature to about 500 K.

We have measured the I-V curves using pre-patterned electrodes with 10 μm interdigitated spacing (NanoSPR, LLC.). A pre-patterned is dipped into a 100 mg/mL gold nanoparticle solution, and the dried film is measured using a Keithley 2400 source meter (Tektronix, Inc.) in the absence of light in a black box. The temperature of the film is varied from room temperature and 383 K using a custom-built heater system, which consists of a strip heater, a temperature controller, and a thermocouple. The I-V characteristics and the temperature-dependent resistance for Au-C_6, Au-C_4, and Au-C_2 films are plotted in Figures 17-19.

The resistance of the Au-C_6 film $R(T)$ changes from 3.0 MΩ at 293 K to 2.25 MΩ at 303 K, which translates to a TCR of

$$\text{TCR} = \frac{1}{R}\frac{dR}{dT} = (3.0 - 2.25)/(3.0 * 10) = 2.5\%. \tag{4.1}$$

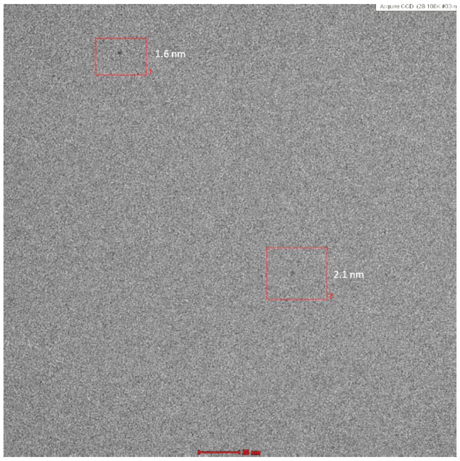

Figure 15: TEM images of Au-TPP obtained at 200K magnification.

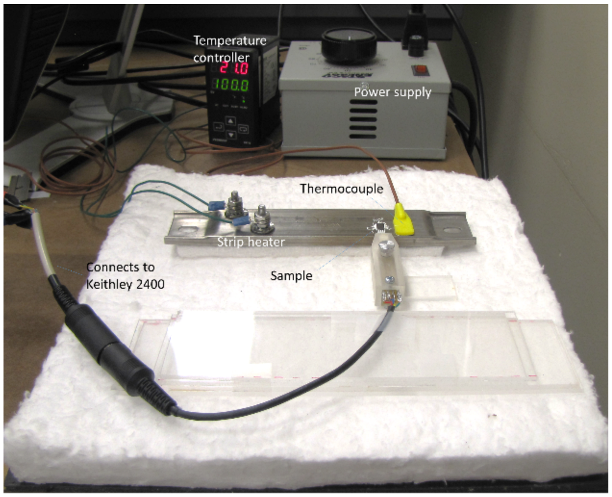

Figure 16: Schematic of apparatus used for I-V characteristic measurements.

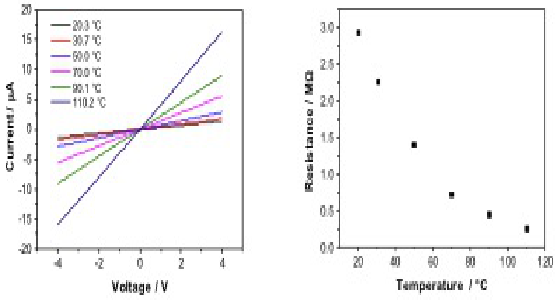

Figure 17: I-V characteristics for different temperatures (a) and device resistance as a function of temperature (b) of Au-C_6 (rgARO44-23) film.

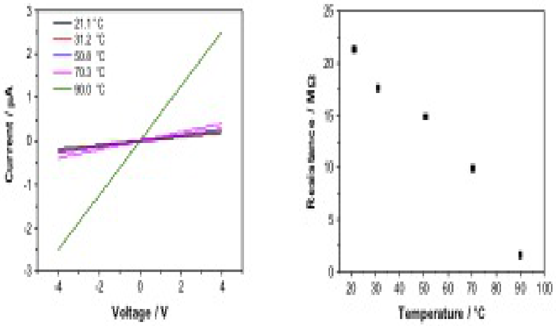

Figure 18: I-V characteristics for different temperatures (a) and device resistance as a function of temperature (b) of Au-C_4 (rgARO69-11) film.

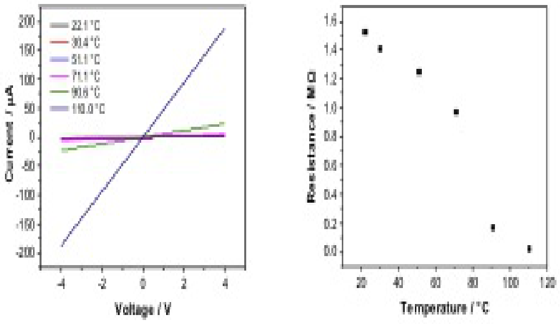

Figure 19: I-V characteristics for different temperatures (a) and device resistance as a function of temperature (b) of Au-C_2 (rgARO47-37a) film.

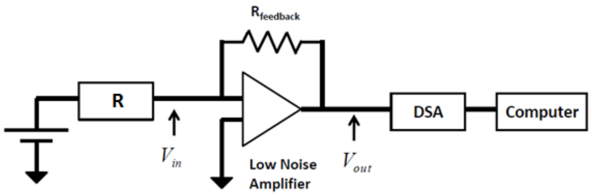

Figure 20: Schematic of apparatus used for noise measurements.

This TCR is comparable to the state-of-the-art value of VO_x. Other films also exhibit a large TCR.

5 Noise measurements

A schematic of the noise measurements is shown in Figure 20. The measured noise is defined as

$$V_m^2 = V(R_F)^2 + (GV_n)^2 \tag{5.1}$$

where $V(R_F)$ is the (Johnson) noise of the amplifier feedback resistor, V_n is the sample noise and G is the amplifier gain. The gain is the ratio of the amplifier output signal voltage, V_{out}, to the input signal voltage, V_{in}, which is equal to the ratio of the feedback resistance to the sample resistance, R.

$$G = V_{out}/V_{in} = R_F/R. \tag{5.2}$$

The system noise is also characterized by using metal film resistors whose resistances are comparable to the devices tested. Using the metal film resistor noise results, the low frequency noise of the cross-linked metal particles film noise and system noise can be quantified.

In general, the total noise measured is comprised of $1/f$ noise, white noise, and Generation-Recombination (G-R) noise, which can be expressed quantitatively as

$$\frac{V_{noise}^2}{\Delta f} = \frac{V_{1/f}^2}{\Delta f} + \frac{V_{white}^2}{\Delta f} + \frac{V_{G-R}^2}{\Delta f}. \tag{5.3}$$

The $1/f$ noise can be described using the Hooge model, with

$$\frac{V_{1/f}^2}{\Delta f} = \frac{\alpha_H}{pV}\frac{V_{Bias}^2}{f^\gamma} \equiv \frac{B}{f^\gamma}, \tag{5.4}$$

where p is the carrier density, V is the device volume, V_{Bias} is the device bias, and γ is the frequency exponent, typically near a value of 1 (in the range from 0.9 to 1.1). The normalized Hooge parameter is α_H/p with α_H being the Hooge coefficient. For the Hooge model, $\sqrt{B} \propto V_{Bias}$ and $B/V_{Bias}^2 \propto 1/V$ for fixed bias voltages.

The G-R noise for a single trap is described by

$$\frac{V_{G-R}^2}{\Delta f} = \frac{A\tau V_{Bias}^2}{1 + (2\pi\tau f)^2}, \tag{5.5}$$

where τ is the trap time constant and $A = n_t/Vp^2$ with n_t being the trap density. The noise waveform for trapping can be analyzed by

$$f\frac{(V_{noise}^2 - V_{white}^2}{V_{Bias}^2} = \frac{\alpha}{pV} + \frac{fA\tau}{1 + (2\pi f)^2}, \tag{5.6}$$

which can be normalized to the device volume with

$$W_N \equiv f\frac{(V_{noise}^2 - V_{white}^2}{V_{Bias}^2}V = \frac{\alpha}{p} + \frac{f(n_t/p^2)\tau}{1 + (2\pi f)^2}. \tag{5.7}$$

Here it is assumed that the exponent of the $1/f$ noise frequency is equal to 1. For the case of a single trap, a plot of of W_N (determined from the measured noise data) yields a horizontal line (of value α_H/p) superimposed with a Lorentzian (trap). Figure 23 shows an example of W_N plot as a function of frequency for noise data taken at different temperatures. For temperatures of 360 K and 380 K, the curves have no slope, indicative that the measured low frequency noise is $1/f$ noise only. The values of these curves are equal to α_H/p. For temperatures 400 K and above, the curves at low frequency (less than 10 Hz) increase with increasing temperature.

Experimental room temperature noise measurements are made in a shielded and light tight enclosure. For temperature dependent noise measurements, the film is mounted within a cryostat. All measurements are made with the films in dark conditions. For noise measurements, a Keithley 428 source is used to bias the device and as a low noise current amplifier. The gain is adjusted by use of a variable feedback resistor within the preamplifier. The amplified signal is converted to a noise voltage - frequency spectrum by a HP 35670A dynamic signal analyzer (DSA). The data is then stored on computer for analysis.

Noise measurements made on two different groups of cross-linked metal particle films Au-C_6 and Au-C_6 (TPP_2) deposited on interdigitated electrodes as shown in Figure 22. The noise measurements were made at Room temperature. The noise data for the films with metal particles rgARO81-1a Au-C_6 is shown in Figure 23. For frequencies greater

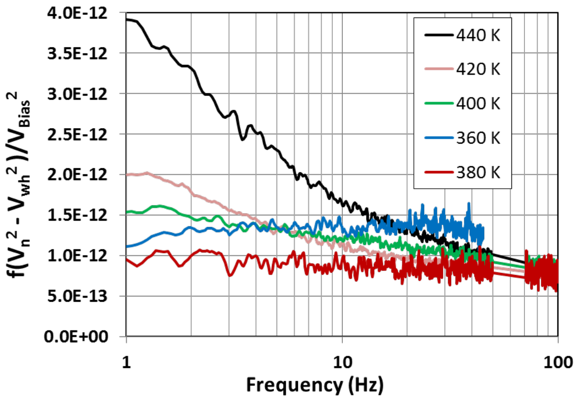

Figure 21: Normalized waveforms analyzed for trapping at various temperatures.

Figure 22: Sample film on a NanoSPR interdigitated electrode.

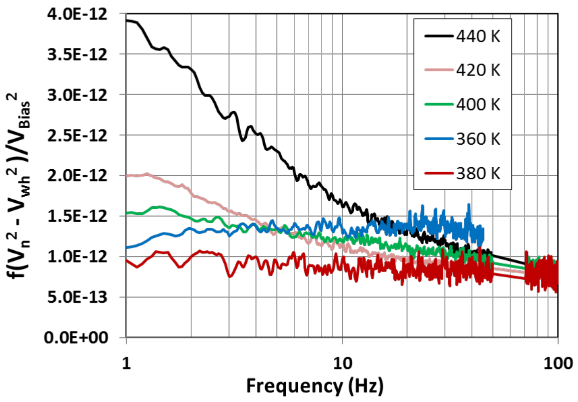

Figure 23: Noise data for sample Au-C_6.

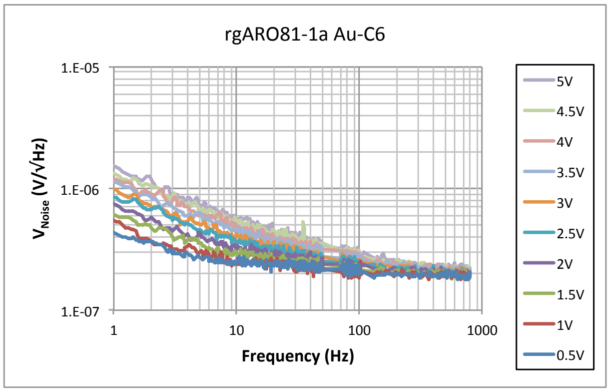

Figure 24: Low-frequency noise data for sample Au-C_6.

than 500 Hz, the noise is white noise. At frequencies less than 100 Hz, the noise is observed to increase with increasing bias voltage.

Figure 24 shows the corresponding low frequency noise (LFN) as a function of frequency for the various bias voltages. The LFN was obtained by appropriately subtracting the white noise from the measured noise. Figure 24 includes the power fit to the data using Eq. (5.4). For frequencies greater than 500 Hz, the noise is white noise. The LFN can be fitted by $1/f^{\gamma}$ with the exponent $\gamma = 0.80$, suggesting that with decrease of the frequency, the LFN increases slower than a typical $1/f$ noise, i.e., the LFN is suppressed as compared to the $1/f$ noise.

6 Conclusions

Our theoretical and experimental results described above indicate that we can synthesize CLMPs with desired particle size based on modeling and can grow high-quality CLMP films. The TCR of the CLMP films is high and comparable to the state-of-the-art VO_x. The low-frequency noise of CLMP films exchibits a weaker frequency dependence than the $1/f$ noise, consistent with our modeling prediction. This weaker frequency dependence promises a low noise level of CLMP films, which, together with the large TCR, suggests that CLMP films have a great potential for uncooled microbolometers, the critical technology for our soldiers.

7 Manuscript submitted

1. **Rashba effect and carrier mobility in hybrid organic-inorganic perovskites**, Z. G. Yu *Journal of Physical Chemistry Letters* **7**, 3078 (2016).
2. **Effective-mass model and magneto-optical properties in hybrid perovskites**, Z. G. Yu *Scientific Reports* **6**, 28576 (2016).
3. **Spin Hall effect in disordered organic solids**, Z. G. Yu *Physical Review Letters* **115**, 026601 (2015).

8 Manuscript in preparation

1. **Synthesis and characterizations of gold nanoparticles array for a high-performance uncooled microbolometer application** R. Gunawidjaja and Z. G. Yu

9 References

1. Boettcher, S. W.; Strandwitz, N. C.; Schierhorn, M.; Lock, N.; Lonergan, M. C.; Stucky, G. D. Nat Mater 2007, 6, 592.

2. Weare, W. W.; Reed, S. M.; Warner, M. G.; Hutchison, J. E. J Am Chem Soc 2000, 122, 12890.